

Practical realization of chiral nonlinearity for strong topological protection

Xinxin Guo,¹ Lucien Jezequel,² Mathieu Padlewski,¹ Hervé Lissek,¹ Pierre Delplace,²
and Romain Fleury^{3, a)}

¹⁾*Signal Processing Laboratory LTS2, Ecole Polytechnique Fédérale de Lausanne,
1015 Lausanne, Switzerland*

²⁾*Univ Lyon, ENS de Lyon, CNRS, Laboratoire de Physique, F-69342 Lyon,
France*

³⁾*Laboratory of Wave Engineering, Ecole Polytechnique Fédérale de Lausanne,
1015 Lausanne, Switzerland*

^{a)}Corresponding author. Email: romain.fleury@epfl.ch

Abstract

Nonlinear topology has been much less inquired compared to its linear counterpart. Existing advances have focused on nonlinearities of limited magnitudes and fairly homogeneous types. As such, the realizations have rarely been concerned with the requirements for nonlinearity. Here we explore nonlinear topological protection through the determination of nonlinear rules and demonstrate their relevance in real-world experiments. We take advantage of chiral symmetry and identify the condition for its continuation in general nonlinear environments. Applying it to one-dimensional topological lattices, we can obtain definite evolution paths of zero-energy edge states that preserve topologically nontrivial phases regardless of the specifics of the chiral nonlinearities. Based on an acoustic prototype design, we theoretically, numerically, and experimentally showcase the nonlinear topological edge states that persist in all nonlinear degrees and directions without any frequency shift. Our findings unveil a broad family of nonlinearities that are compatible with topological nontriviality, establishing a solid ground for future drilling in the emergent field of nonlinear topology.

Main

Topological protection has received a surge of interest owing to its strong immunity to parametric perturbations and geometrical defects. It has been investigated on versatile platforms, from quantum mechanics¹ to multifarious classical realms such as electronics^{2–5}, photonics^{6–10} and phononics^{11–20}. In contrast to the tremendous attention paid to linear physics and band theory, topological research has less accented on the intersections with nonlinear dynamics^{10,21,22}, despite the ubiquity of nonlinearity in nature. Various nonlinear sources have been exploited for topological purposes, including varactor diodes inserted in electrical circuits^{4,5,23–25}, optical materials with intensity-dependent refractive index^{10,26–28}, geometry^{29,30} or nonlinear stiffness^{31–33} of mechanical structures, and active means that create nonlinearity together with non-Hermiticity³⁴. However, the types of nonlinearities are rather homogeneous in previous surveys, with a strong dominance of Kerr-like onsite nonlinearities^{5,6,10,23,26,27,31,33,35–42}, due to their ease in passive realizations and the link to bosonic quantum systems through the well-known Gross-Pitaevskii equation⁴³. Exceptions arise mainly from the use of specific lasers^{28,34} or electrical elements^{4,25}, whose self-focusing or defocusing behaviors are described by saturable nonlinear gains.

The nonlinear effects, once triggered, have resulted in topologically nontrivial phases that were mostly trivial in the linear regime^{10,22}, allowing for many fascinating phenomena such as first- or second-order topological insulators^{5,26,32,39}, soliton propagation^{27–29,31,37,44,45}, and higher harmonic generations^{24,46–48}. Nevertheless, studies reported to date possess their own specific effective range of nonlinearities. Some of them have been restricted to weak nonlinear magnitudes to approach theoretical models and/or to enable theoretical analyses (viable linearization and perturbation methods)^{4,5,31,35,40,46}. Others, on the other hand, have required nonlinearity strong enough to activate nonlinear states (e.g., solitons) or to localize them clearly (e.g. corner topological states). A few have explored large intervals of nonlinear levels from low to high (before chaos), but with the edge modes/states shifted in frequency^{23,33,36,38,49}, ultimately destroying topological phases due to nonlinearity-induced symmetry breaking. Nonlinear topology, discovered within limited contents and extents of nonlinearity, has hardly been discussed from a fundamental nonlinear perspective thus far. That is, taking the stand on topological demands, what nonlinearities are actually needed? Is it feasible in practice to keep topological attributes intact across all nonlinear magnitudes?

To tackle the question, here we unlock limitations to the manipulation of nonlinear topological systems in theory and practice, by satisfying a symmetry that maintains topological non-triviality permanently. Different types of symmetries can enable topological phases of matter^{6,12,50}, including time-reversal symmetry⁵⁰, reflection symmetry⁵¹, Parity-Time symmetry³⁴, chiral symmetry^{52,53} or derived sub-symmetries⁵⁴. Our study utilizes chiral symmetry that is closely related to the emergence of zero-energy topological edge states⁵⁵. We first identify the nonlinear condition for symmetry preservation in general periodic systems. We then introduce eligible nonlinearities in one-dimensional (1D) lattices to alter the linearly produced stationary topological edge states, considering a general monotonic amplitude dependence of the nonlinearity. A concrete nonlinear case is finally examined in a theoretical lumped element circuit and in an equivalent real active nonlinear acoustic system. We confirm theoretically, numerically, and experimentally that under chiral nonlinearities, nonlinear edge states can sustain their topologically nontrivial phases while never shifting in frequency.

Chiral symmetry for general nonlinear periodic systems

A previous theoretical study⁵³ has given nonlinear laws for the fulfillment of chiral symmetry, dedicated to $\mathbf{H}|\Psi\rangle$, the product of the Hamiltonian \mathbf{H} and the wave function Ψ . In terms of the Hamiltonian \mathbf{H} of the system, and in the presence of arbitrary nonlinearities and non-localities depending on the different degrees of freedom (a_i, b_j, c_k, \dots) contained in the system, chiral symmetry implies that $\Gamma\mathbf{H}(a_i, b_j, c_k, \dots)\Gamma^\dagger = -\mathbf{H}(a_i, b_j, c_k, \dots)$, with Γ the chiral operator and \dagger the conjugate transpose. In the chiral base of the degrees of freedom, where $\Gamma = \begin{bmatrix} 1_a & 0 \\ 0 & -1_b \end{bmatrix}$ with 1_a and 1_b the identity matrices of random sizes, this definition is equivalent to say that $\mathbf{H}(a_i, b_j, c_k, \dots)$ is block off-diagonal, namely

$$\mathbf{H}(a_i, b_j, c_k, \dots) = \begin{bmatrix} 0 & h(a_i, b_j, c_k, \dots) \\ h^\dagger(a_i, b_j, c_k, \dots) & 0 \end{bmatrix}. \quad (1)$$

Notably, there are no specific restrictions on the nonlinearities in $h(a_i, b_j, c_k, \dots)$ in Eq. (1). They can, in principle, take any form and rely on different elements of the system at will, even in a non-local way. The only requirement is that the sites of the same chirality must be uncoupled from each other. Conversely, any nonlinearity that creates couplings

among them will inevitably cause the breaking of the symmetry, such as the Kerr onsite nonlinearity that has been extensively inquired. Here using Eq. (1), the aim is to find ways to retain chiral symmetry over all nonlinear magnitudes and directions.

Generalized nonlinear topological protection with chiral symmetry

The satisfaction of Eq. (1) allows for chiral symmetry in systems of any dimension. For a direct application, we focus on the zero-energy edge states in 1D dimerized lattices, where Eq. (1) is already met by the Hamiltonian in the natural base. We start with the linear chiral case, in which the system dynamics are governed by the Schrödinger equation. Taking the energy terms equal to zero, one gets $\eta_L a_n + a_{n+1} = 0$ and $\eta_L b_n + b_{n-1} = 0$, where a_n and b_n are the amplitudes in the two sites of the n -th unit cell, and the N complex amplitudes a_n (b_n) constitute the entire sublattice A (B) of the system. A topologically nontrivial phase is obtained if the hopping ratio η_L (ratio between the hopping terms, see Method) is smaller than one. The resulting linear topological edge state is displayed in Fig. 1, where the sites a_n carry a decrease in amplitudes along A, with the descent rate fixed by η_L . The presence of chiral symmetry makes the sites b_n stay stationary, independent of a_n .

When nonlinearities get involved in a way that respects Eq. (1), the system energy relations become:

$$0 = a_{n+1} + [\eta_L + \eta_{NLa}(a_{n+i}, b_{n+j})] a_n, \quad 0 = b_{n-1} + [\eta_L + \eta_{NLb}(a_{n+k}, b_{n+l})] b_n, \quad (2)$$

This suggests that, under chiral symmetry, the participation of nonlinearity results only in modifications in the hopping ratios. They are transformed from the linear invariant η_L to the amplitude-dependent nonlinear variables $\eta_L + \eta_{NLa}(a_{n+i}, b_{n+j})$ applied to a_n and $\eta_L + \eta_{NLb}(a_{n+k}, b_{n+l})$ applied to b_n . a_{n+i} and b_{n+j} (a_{n+k} and b_{n+l}) refer to each site that the nonlinearity in η_{NLa} (η_{NLb}) depends on. They can be arbitrary in the system, i.e., the integer i or j or k or l can be zero if the dependency occurs within the n -th unit cell, or nonzero if the dependency is on the other interacting unit cells.

We assume the most common form of chiral nonlinearity, namely with monotonic changes in the hopping ratios as the site amplitudes increase. We first deal with the classical ones that are positively correlated with amplitudes. Based on $a_n > a_{n+1}$ of the linear state, these

nonlinearities lead to $|\eta_{\text{NL}a}(a_{n+i}, b_{n+j})| > |\eta_{\text{NL}a}(a_{n+1+i}, b_{n+1+j})|$ in the early nonlinear stage (negligible effects of sites in B, since they carry zero amplitude linearly), where the sign of $\eta_{\text{NL}a}$ determines whether nonlinearity increases or decreases the hopping ratios on A. If $\eta_{\text{NL}a} < 0$, we have $\eta_L + \eta_{\text{NL}a}(a_{n+i}, b_{n+j}) < \eta_L + \eta_{\text{NL}a}(a_{n+1+i}, b_{n+1+j}) < \eta_L < 1$, i.e., the hopping ratios are diminished by nonlinearity, with the decrement less and less along A. As nonlinearity is further strengthened, its positive dependence on amplitudes perpetuates the above law. The first hopping ratio remains thus the smallest, always yielding the largest reduction of amplitude from a_1 to a_2 . Following this trend, we reach a limit situation where solely the first site a_1 has a nonzero amplitude. The sites b_n in B remain at zero amplitude, owing to chiral symmetry and to the fast decay of the nonlinear mode that prevents it from reaching the other end of the system. The total expected edge state variations for nonlinearity decreasing the hopping ratios on A ($\eta_{\text{NL}a} < 0$) are depicted graphically in the lower branch in Fig. 1.

The reasoning applies likewise to the opposite scenario of $\eta_{\text{NL}a} > 0$, where the derived $|\eta_{\text{NL}a}(a_{n+i}, b_{n+j})| > |\eta_{\text{NL}a}(a_{n+1+i}, b_{n+1+j})|$ results in $\eta_L + \eta_{\text{NL}a}(a_{n+i}, b_{n+j}) > \eta_L + \eta_{\text{NL}a}(a_{n+1+i}, b_{n+1+j}) > \eta_L$, i.e., the hopping ratios are increased by nonlinearity, with the increment smaller and smaller along A. Remarkably, the first ratio is the largest here, contrary to the previous case of $\eta_{\text{NL}a} < 0$. The enhancement of nonlinearity impels it to first attain 1, at which moment the site a_2 acquires the same amplitude as a_1 . After that, if nonlinearity still can increase the hopping ratio, a_2 exceeds a_1 in amplitude. The continuation along this direction makes the ascent of a_2 incessant and towards an infinite level, which will inevitably end with instability of the system. For this reason, to allow stable states at all nonlinear magnitudes, the nonlinearity should always keep the first hopping ratio at 1 once $a_2 = a_1$ is reached. The other hopping ratios follow the same result due to the periodicity of the system. That is, for $\eta_L + \eta_{\text{NL}a}(a_{n+i}, b_{n+j})$ applied to a_n , we have $\eta_L + \eta_{\text{NL}a}(a_{n+i}, b_{n+j}) = 1$ once $a_{n+1} = a_n$. Such a relationship easily holds if the hopping terms for a_n and a_{n+1} are both nonlinear and dominated by the amplitudes of a_n and a_{n+1} , respectively, as exemplified by the explicit case in Fig. 2a (Method). It shows that, as the nonlinearity strengthens, the sites a_n ($n \geq 2$) successively arrive at the amplitude of a_1 and then sustain there. Ultimately, they will exhibit the same amplitude, forming a 'plateau' in A.

For actual systems with finite dimensions, the zero-energy mode reaches the other edge of the system when all sites in A are nonlinearly endowed with nonzero amplitudes. In

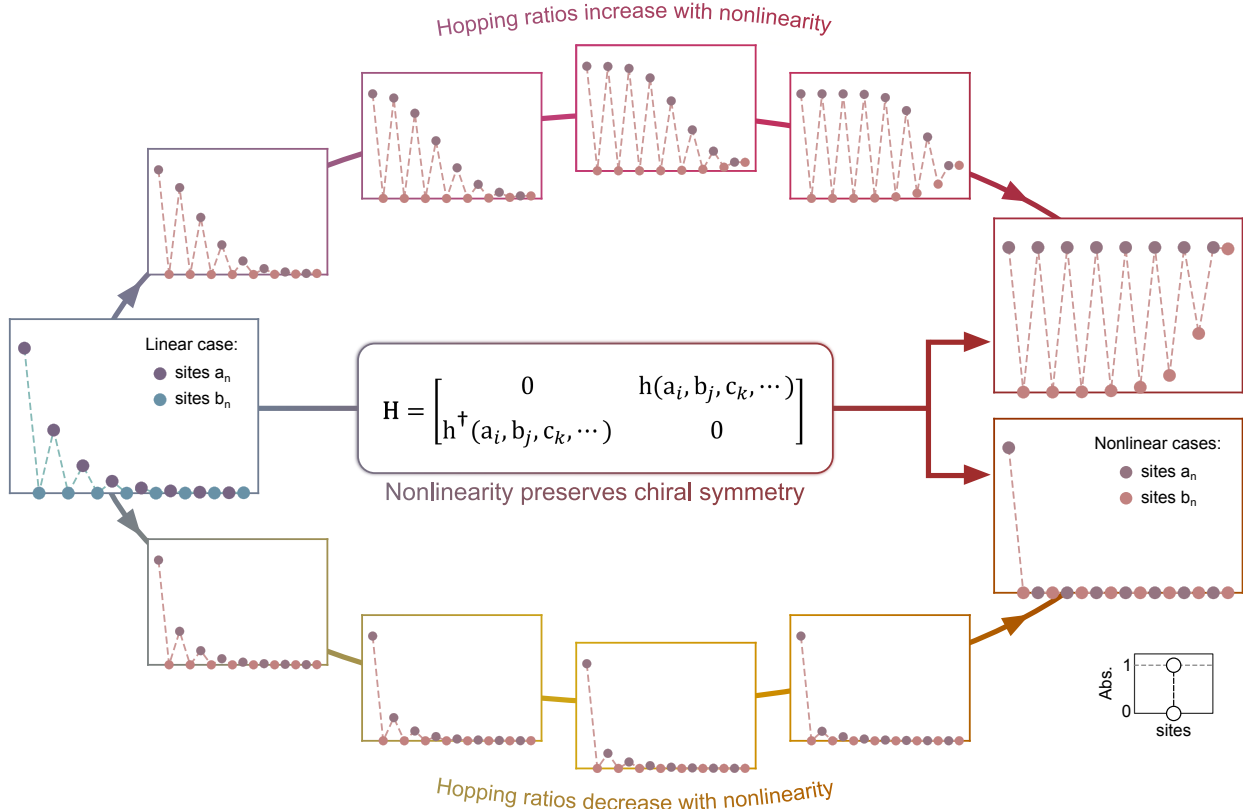


FIG. 1. **Expected qualitative evolution laws for zero-energy edge states in 1D dimerized systems with symmetry-preserving nonlinearities.** Profiles of the zero-energy edge state that is initially (linearly) topological and then varied as chiral nonlinearities increase and decrease the hopping ratios on sublattice A, respectively. In each profile, the amplitude of the first site a_1 is fixed at 1. The requirement on the Hamiltonian \mathbf{H} is explained in Eq. (1).

this case, the excited opposite zero mode causes the amplitude of the sites in B to begin to rise, with a lowering from b_n to b_{n-1} , i.e., a heightening along the structure. No conclusion can be drawn about the direction of changes in the hopping ratios on B. Their increase or decrease are separate from those on A, as Eq. (1) states. Despite this, it is certain that from an initial value of less than 1, the nonlinearity should drive the hopping ratios up to 1 at most, as we discovered earlier through the sublattice A. The extreme nonlinear result can hereby be extrapolated: sites b_n conduct an increase in amplitude along B, with merely the first b_1 at rest. Our overall estimates for the case of nonlinearity increasing the hopping ratios on A ($\eta_{\text{NL}a} > 0$) are delineated schematically in the upper branch in Fig. 1, where the pattern in B results from the explicit nonlinearity considered later in Fig. 2a.

Performing the same analysis as above for nonlinearities that are negatively correlated with site amplitudes, one will obtain the same evolution limits as in Fig. 1. Collectively, accounting for a monotonic amplitude dependence of the chiral nonlinearity, the hopping ratios can always stay smaller than or at most equal to 1 for both sublattices A and B. Therefore, the derived variation tendencies lead to the nonlinear edge states that remain topologically nontrivial, whatever the nonlinear contents. A result similar to part of Fig. 1 was previously observed in a numerical attempt³¹, but with a particular nonlinear management and without discussing the underlying symmetry cause. Distinctively, here our starting point is to interrogate chiral symmetry, thus unveiling the entire class of nonlinearities that ensures topological non-triviality.

Example of nonlinear topological protection with chiral symmetry

To confirm our anticipations in Fig. 1, we take the example of a concrete finite system represented by the lumped element circuit in Fig. 2a. It consists of 8 unit cells, each with linear and nonlinear resonators. The linear resonators LF_{2k-1} and LF_{2k} are identical and exhibit a resonance at a lower frequency f_{LF} . The nonlinear resonators HF_{2k-1} and HF_{2k} resonate at the same frequency f_{HF} , higher than f_{LF} , while a larger (linear) resonance bandwidth is assigned to HF_{2k-1} compared to HF_{2k} . The generators $V_{2k-1}^{(\text{NL})}$ ($V_{2k}^{(\text{NL})}$) introduce nonlinearity into HF_{2k-1} (HF_{2k}), with the explicit nonlinear laws given also in Fig. 2a. The overall system allows stationary topological edge states at two different frequencies (see Extended Data Fig. 1 and Method), dominated by the resonance of LF_n and HF_n ($n = 2k-1$ and $2k$), respectively. The voltages carried by LF_{2k-1} (LF_{2k}) correspond to the amplitudes of sites a_n (b_n). In the linear regime, the hopping terms for a_n (b_n) and a_{n+1} (b_{n-1}) are directly mapped to the capacitances $C_{2k-1}^{(\text{HF})}$ in HF_{2k-1} and $C_{2k}^{(\text{HF})}$ in HF_{2k} (Supplementary Note 1.1). In the nonlinear regime, instead, they are dictated by the nonlinearity engaged. Their amplitude dependence is complex: it is not only on the sites a_n and b_n inside the associated n -th unit cell, but also on the sites b_{n-1} and a_{n+1} in the adjacent ones (Method). Despite this complexity, the chosen nonlinearities are rigorously chiral.

Our attention is devoted to the topological edge state where the resonance of HF_n prevails. Its nonlinear evolution is revealed in Fig. 2b. In the initial linear scenario, the hopping ratio

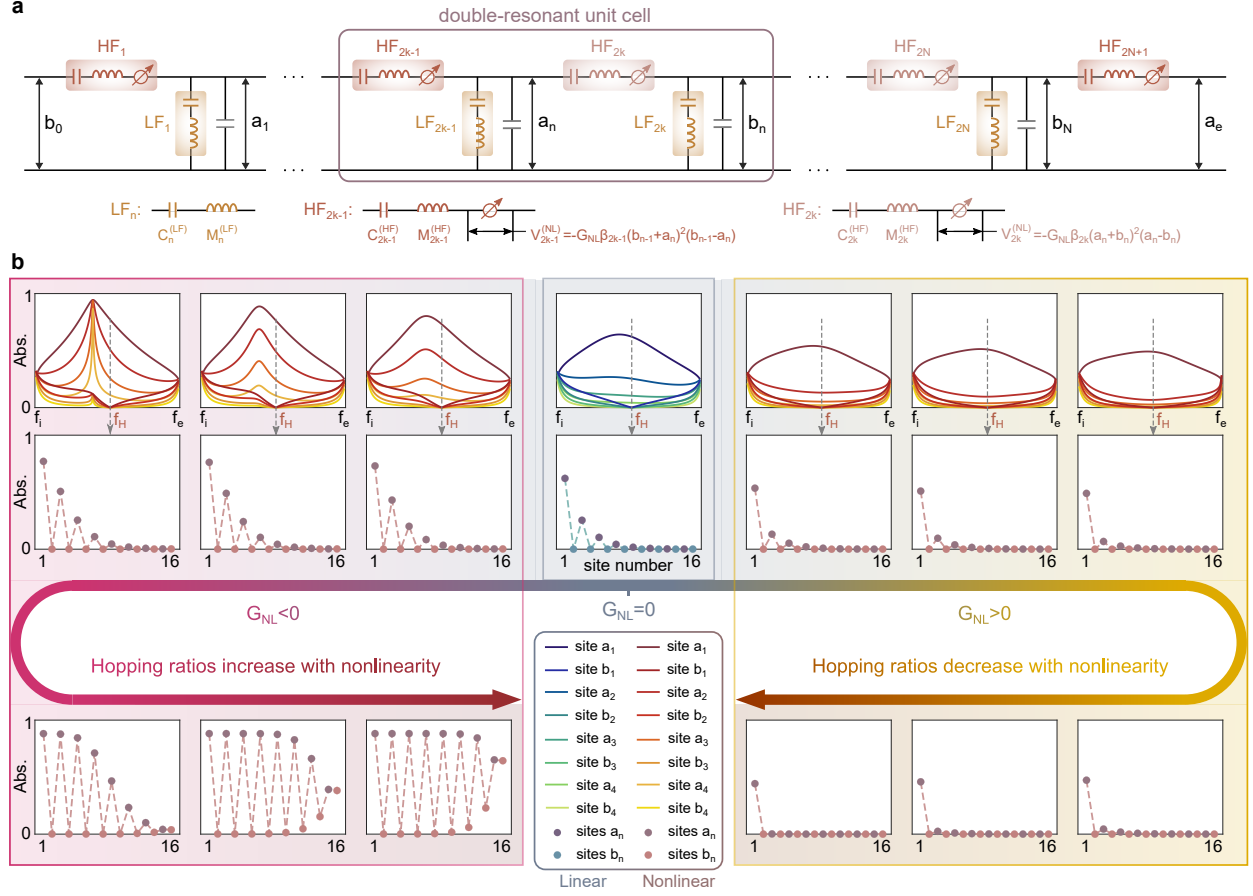


FIG. 2. Evolution of the chiral symmetry protected nonlinear topological edge states: theoretical demonstration in a lumped element circuit with coupled resonators. **a**, The considered 1D nonlinear system. It is made of 8 unit cells, each composed of 2 linear resonators LF_n and 2 nonlinear resonators HF_n ($n = 2k - 1$ and $2k$). Nonlinearity is added in HF_n through the generators $V_n^{(NL)}$. **b**, Nonlinear variations of the linearly generated stationary topological edge state, under the intervention of the nonlinearity given in **a**. The nonlinear levels and directions are tuned by the constant parameter G_{NL} in the nonlinear law. It increases (decreases) the hopping ratios on sublattice A with $G_{NL} < 0$ ($G_{NL} > 0$), The spectra of a_n and b_n ($n = 1, 2, 3, 4$) in the frequency range of $[f_i, f_e]$ are utilized for the identification of the edge state frequency f_H . All the figures are displayed in the same amplitude range and normalized to the maximum value. Results are obtained with the Harmonic Balance Method (see Method), and more cases are given in Extended Data Fig.2. Time domain analysis with the time-integration method is outlined in Supplementary Note 1.2.

is defined at around 0.41 (equal to $C_{2k}^{(\text{HF})}/C_{2k-1}^{(\text{HF})}$). The edge state frequency f_{H} is recognized from the site spectra in Fig. 2b, at the zero amplitudes of all sites b_n . Nonlinearity is then activated and prescribed using the constant parameter G_{NL} in the nonlinear law. When G_{NL} is decreased along negative values, the hopping ratios on sublattice A are gradually enlarged. The first ratio keeps receiving the greatest increment. It takes the lead to reach 1, followed by the others in succession. At the very end, the plateau on A is infinitely approached, with solely the last hopping ratio still small. Conversely, in the direction $G_{\text{NL}} > 0$, nonlinearity incessantly reduces the hopping ratios on A. The relative descent (with respect to the former site) of a_2 remains the largest compared to the other sites. The extreme case of only a_1 surviving is also attained. As for the sites b_n in B, their amplitudes rise exclusively after the activation of the opposite zero mode (along $G_{\text{NL}} < 0$), presenting the expected increasing order from b_1 to b_8 .

Thanks to the chiral symmetry of our system, the edge state is conserved at its linearly produced frequency f_{H} , as can be seen from Fig. 2b. It constantly holds a topologically non-trivial phase, as the nonlinear hopping ratios never exceed 1. On the contrary, if nonlinearity breaks the symmetry, the movements of A and B join each other, which causes the edge state to be distorted in shape and shifted in frequency. Additionally, the site spectra in Fig. 2b evidence that the amplitude relation of $a_{n+1} < a_n$ is linearly valid over the entire frequency range of $[f_i, f_e]$ displayed therein. It can be nonlinearly transformed up to $a_{n+1} = a_n$ only, as we proved with the state at f_{H} . Not surprisingly, if nonlinearity is further enhanced from an already reached $a_{n+1} = a_n$, instability would occur at the related frequency. The leftmost spectra in Fig. 2b corresponds to the stability limit of this situation, where the site a_1 is caught up by a_2 at a frequency different from f_{H} . However, the nonlinear edge state at f_{H} is perpetually stable, since its variations always satisfy $a_{n+1} \leq a_n$. As a result, the nonlinear case in Fig. 2b fully demonstrates our inferences for the general context of nonlinearity.

Experimental validations

After exploration of the theoretical lattice in Fig. 2, an equivalent active nonlinear acoustic system is adopted for experimental validation, as pictured in Fig. 3a. A waveguide is used for connecting all the elements. Passive Helmholtz resonators are mounted on its (top) side to play the role of the linear LF_n , while electrodynamic loudspeakers are inserted inside

and are actively controlled to act as the nonlinear HF_n . The control for each loudspeaker involves a feedback loop, where a time-dependent nonlinear control law is appropriately defined based on the acoustic pressures measured on both faces of the loudspeaker membrane (Method and Extended Data Fig. 3). The control output is returned to the loudspeaker terminals in real-time in the form of a drive current, achieving active resonators HF_n with fully adjustable and reconfigurable characteristics. A total of 8 unit cells are constructed in experiments, each composed of two equally spaced Helmholtz resonators and two equally spaced active loudspeakers. The sub-wavelength portions of tube V_a , enclosed by adjacent speakers, behave similarly to capacitors. Accordingly, the system in Fig. 3a realizes the theoretical lattice in Fig. 2a.

The same investigations as in the theoretical studies are performed experimentally. First, the topological edge state is successfully implemented in the linear case, as illustrated in Fig. 3b (detailed results in Extended Data Fig. 4). A hopping ratio of around 0.54 is obtained, not very far from the theoretical one of 0.41 (in Fig. 2b). The discrepancy stems from the approximation of each space V_a as a lumped element (see proof with simulations in Supplementary Note 2). Based on the linear results, nonlinearity is added to the system and tailored by the constant parameter G_{NL} , as theoretically set in Fig. 2b. When nonlinear magnitude is reinforced along $G_{\text{NL}} < 0$, the hopping ratios on A increase. The sites a_n sequentially attain the same level, enabling the theoretical plateau limit at the greatest extent of nonlinearity. In the meantime of the ascent on sublattice A, the sites in B first remain at rest and then rise in amplitude from the last one b_8 , which comply also with the theoretical projections.

For nonlinearity decreasing the hopping ratios with $G_{\text{NL}} > 0$, the shape of the edge state is centralized more and more on the structure (left) end, with all sites in B staying stationary. The nonlinear variation along this direction proceeds until the first hopping ratio (the smallest one) on A falls to about 0.2, with respect to the linear one of 0.54. The limit of only a_1 being dynamic cannot be observed, as instability arises first, which is in accordance with time-domain analysis (theoretical and numerical in Supplementary Notes 1.2 and 2, respectively). Nevertheless, all expected laws of variations are exhaustively justified by experiments. The realized nonlinear topological edge states are negligibly affected by losses in the system. They preserve topologically nontrivial phases and with unchanged frequency at f_{H} , since chiral symmetry is here rigorously obeyed by nonlinearity.

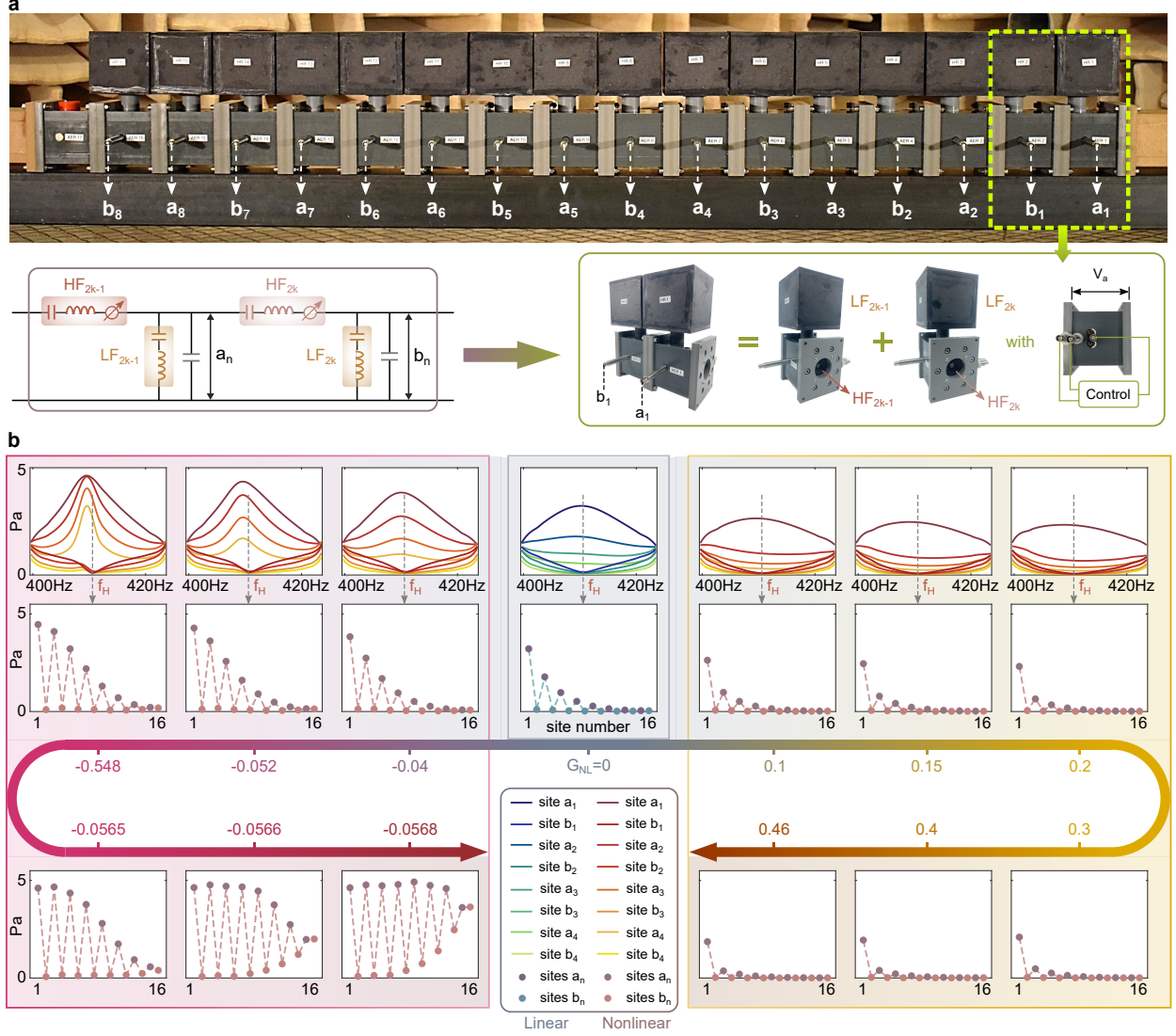


FIG. 3. Evolution of the chiral symmetry protected nonlinear topological edge state: experimental validation in an active nonlinear acoustic system. **a**, The actual system that realizes the theoretical lattice in Fig. 2a. The unit cell consists of two passive linear Helmholtz resonators (acting as LF_n) and two active nonlinear loudspeakers (acting as HF_n). The whole system starts and ends both with the controlled loudspeakers. **b**, Nonlinear topological edge states, measured as nonlinearity is progressively altered using the constant control parameter G_{NL} . The hopping ratios on sublattice A are increased (decreased) along $G_{NL} < 0$ ($G_{NL} > 0$). The edge state frequency f_H is identified from the spectra of a_i and b_i ($i = 1, 2, 3, 4$). Experimental results of more cases are given in Extended Data Figs. 5 and 6.

Discussion

In this study, we explored the nonlinear possibilities for the persistence of topological non-triviality. We targeted the symmetry-protected topological class and put the emphasis on chiral symmetry. The condition to secure symmetry was first formulated for general nonlinear periodic systems. It was then applied to one-dimensional lattices in which zero-energy topological edge states were modified by arbitrary nonlinearities with chiral symmetry. The trajectories of their nonlinear evolution were predicted based on a monotonic amplitude dependence of the nonlinearities. The results show that chiral nonlinearities can consistently maintain the edge states in a topologically nontrivial phase, regardless of the explicit nonlinear form and magnitude. The derived nonlinear topological edge states were put into practice through the consideration of a concrete finite system, with theoretical representation in a lumped element circuit, and with numerical (Supplementary Note 2) and experimental implementations in an equivalent active nonlinear acoustic system. By virtue of chiral symmetry, our investigations reveal a broad class of nonlinearities that keep the topological attributes intact and the edge state frequency unshifted over all nonlinear magnitudes, opening up new avenues of thought for the continued study of nonlinear topology.

Method

Lumped element circuit

The dynamics of the lumped element circuit in Fig. 2a is described by

$$\begin{cases} \Delta_t^{(\text{HF})} q_{2k-1} = C_{2k-1}^{(\text{HF})} (b_{n-1} - a_n) + G_{\text{NL}} C^{(\text{HF})} (b_{n-1} + a_n)^2 (b_{n-1} - a_n), \\ \Delta_t^{(\text{HF})} q_{2k} = C_{2k}^{(\text{HF})} (a_n - b_n) - G_{\text{NL}} C^{(\text{HF})} (a_n + b_n)^2 (a_n - b_n), \\ \Delta_t^{(\text{LF})} \left(q_{2k-1} - q_{2k} - q_{2k-1}^{(a)} \right) = C_{2k-1}^{(\text{LF})} a_n, \\ \Delta_t^{(\text{LF})} \left(q_{2k} - q_{2k+1} - q_{2k}^{(a)} \right) = C_{2k}^{(\text{LF})} b_n, \end{cases} \quad (3)$$

where q_{2k-1} , q_{2k} and $q_n^{(a)}$ ($n = 2k - 1$ and $n = 2k$) designate the charges of the resonators HF_{2k-1} , HF_{2k} and the capacitor in parallel with LF_n , respectively. $\Delta_t^{(\text{HF})}$ and $\Delta_t^{(\text{LF})}$ denote the time-domain differential operators with explicit expressions given in Supplementary Note

1.1. $C^{(\text{HF})}$ is the average of the capacitors $C_{2k-1}^{(\text{HF})}$ and $C_{2k}^{(\text{HF})}$. The equivalence to a 1D topological lattice is identified at two different frequencies (Extended Data Fig. 1), denoted as f_{H} and f_{L} . The relations in Eq. (2) are enabled with the hopping ratios $\eta_{\text{L}} + \eta_{\text{NL}a}$ and $\eta_{\text{L}} + \eta_{\text{NL}b}$ in the forms of

$$\eta_{\text{L}} + \eta_{\text{NL}a} = \frac{t_{0a}(a_n, b_n)}{t_{1a}(a_{n+1}, b_n)}, \quad \eta_{\text{L}} + \eta_{\text{NL}b} = \frac{t_{0b}(b_n, a_n)}{t_{1b}(b_{n-1}, a_n)}. \quad (4)$$

t_{0a} (t_{0b}) and t_{1a} (t_{1b}) are the hopping terms for the sites a_n (b_n) and a_{n+1} (b_{n-1}), respectively, which read,

$$\begin{cases} t_{1a}(a_{n+1}, b_n) = C_1^{(\text{HF})} + G_{\text{NL}}C^{(\text{HF})} (a_{n+1}^2 + b_n a_{n+1} - b_n^2), \\ t_{0a}(a_n, b_n) = C_2^{(\text{HF})} - G_{\text{NL}}C^{(\text{HF})} (a_n^2 + b_n a_n - b_n^2), \\ t_{1b}(b_{n-1}, a_n) = C_1^{(\text{HF})} + G_{\text{NL}}C^{(\text{HF})} (b_{n-1}^2 + a_n b_{n-1} - a_n^2), \\ t_{0b}(b_n, a_n) = C_2^{(\text{HF})} - G_{\text{NL}}C^{(\text{HF})} (b_n^2 + a_n b_n - a_n^2), \end{cases}$$

with $C_1^{(\text{HF})} = C_{2k-1}^{(\text{HF})}$ and $C_2^{(\text{HF})} = C_{2k}^{(\text{HF})}$.

Boundary conditions

Theoretically, in order to obtain the edge states, we require that the boundaries b_0 and a_e of the lumped element circuit in Fig. 2a satisfy $b_0 = a_e = 0$. However, this is not directly achievable in practice, especially for the acoustic system we chose for the experiments. In our search for applicable boundary conditions, we eventually found that the typical Non-Reflecting Boundary Conditions (NRBCs) in planar acoustic wave propagation can replace the ideal ones, as proved in Extended Date Fig. 7. They are thus undertaken for all the studies of the concrete theoretical model and the equivalent experimental system.

Theoretical solution

To solve the Eq. (3) describing the theoretical model, we exploit both the harmonic balance method⁵⁶⁻⁵⁸ and the time-integration method⁵⁹ which are standard for solving nonlinear differential equations. They are capable of handling strong levels of nonlinearities, in contrast to the perturbation method and the method of multiple scales that are valid only at weak nonlinearities. The key features of each method are explained shortly in the following.

Harmonic balance method

The results in Fig. 2b are steady-state solutions (with no consideration of transient responses) derived using the semi-analytical Harmonic Balance Method (HBM)⁵⁶⁻⁵⁸. The first 27 harmonics are taken into account for each variable. The detailed results (more cases than in Fig. 2b) are summarised in Extended Data Fig. 2.

Time integration method

The time integration method, with the fourth-order Runge-Kutta (RK4), is utilized to solve the problem numerically and to account for the transient responses. The corresponding results are given in Supplementary Note 1.2.

Time-domain simulation of the experiments.

To better guide and analyze the experiments, we performed time-domain simulations for the active nonlinear acoustic system built in practice. The approach involves a Finite Difference Time Domain (FDTD) method by discretization of the 1D wave equations. Practical details are accounted for in the simulations, that is (i) we consider the wave propagation inside each space between two nearby loudspeakers (with FDTD), (ii) we add the losses in all resonant elements and transmission lines according to the experimentally estimated values, (iii) the actual active control on each loudspeaker, with the control principle and laws explained in the following Method section for experiments (Eqs. (5) and (6) with $i(t)$ changing to $i(t - \tau)$, and with $\tau = 100 \mu\text{s}$). Regarding the numerical settings, we take randomly the experimental values of one loudspeaker to define all the others. The simulation outcomes are summed up in Supplementary Note 2. They are essentially identical to the experimental ones. For the sake of brevity, they are not showcased here.

Characterisations of the experimental setup

In the experimental setup, NRBCs are achieved with anechoic terminations at both ends of the system, which are qualified by absorption coefficients higher than 0.998 from 140 Hz (less than 5% of reflection). The waveguide in Fig. 3a refers to a PVC duct with a cross-sectional

area of $6\text{ cm} \times 6\text{ cm}$, which ensures planar wave propagation until 2.86 kHz. The manufactured Helmholtz resonators (labeled with HR_n in Fig. 3a) reach a transmission coefficient of around 0.008 at their resonance frequencies in the range of [110.5 Hz, 111.5 Hz], corresponding to an acoustic resistance of $0.005Z_c$ with Z_c the specific acoustic impedance of the air. The electrodynamic loudspeakers are all the same commercially available Visaton FRWS 5 SC model, while they actually possess different resonance frequencies (within [345 Hz, 375 Hz]) and bandwidths, which we calibrated beforehand.

Active control on the electrodynamic loudspeakers.

The loudspeaker membrane behaves as a mass-spring-damper system in the linear regime (weak input levels). The motion equation for its displacement ξ read

$$M_{\text{ms}} \frac{\partial^2}{\partial t^2} \xi(t) + R_{\text{ms}} \frac{\partial}{\partial t} \xi(t) + \frac{1}{C_{\text{ms}}} \xi(t) = p_{\text{tot}}(t) S_d - \text{Bli}(t), \quad (5)$$

In the passive open-circuit case, the membrane is subject to the total acoustic pressure p_{tot} over its effective surface area S_d , and the mechanical forces which rely on the mechanical mass M_{ms} , resistance R_{ms} , and compliance C_{ms} . Its dynamics are characterized by a specific acoustic impedance Z_s (ratio between acoustic pressure and velocity) in the frequency domain, $Z_s(j\omega) = \frac{1}{S_d} \left(j\omega M_{\text{ms}} + R_{\text{ms}} + \frac{1}{j\omega C_{\text{ms}}} \right)$.

The active control on each loudspeaker is implemented by specifying the current $i(t)$, which creates an electromagnetic force through the moving coil with a force factor of Bl . The control approach is depicted in detail in Extended Data Fig. 3, where the control law is digitally defined with a Speedgoat real-time target machine manipulated in the Simulink environment of MATLAB. It produces the current $i(t)$ in the form of,

$$i(t) = \mathcal{F}^{-1}(\Phi(j\omega) \cdot P_{\text{tot}}(j\omega)) + \mathcal{F}^{-1} \left(\frac{S_d}{\text{Bl}} - \Phi(j\omega) \right) * \left((-1)^n \frac{C^{(\text{exp})}}{C_n^{(\text{exp})}} G_{\text{NLP}_{\text{tot}}}(t) (p_f(t) + p_b(t))^2 \right), \quad (6)$$

where p_f and p_b are the acoustic pressures measured at the front and rear faces of the loudspeaker membrane, which are the two inputs for the control. \mathcal{F}^{-1} and the symbol $*$ designate the inverse of the Fourier Transform and the time convolution, respectively. The total acoustic pressure p_{tot} reads $p_{\text{tot}} = p_f(t) - p_b(t)$, with $P_{\text{tot}} = \mathcal{F}(p_{\text{tot}})$ its Fourier transform. $C_n^{(\text{exp})}$ refers to the acoustic compliance achieved for the n -th loudspeaker which differs between $n = 2k - 1$ and $n = 2k$, and $C^{(\text{exp})}$ is the average of two successive ones, they

are equivalent to the electrical capacitors $C_1^{(\text{HF})}$ for $n = 2k - 1$, $C_2^{(\text{HF})}$ for $n = 2k$, and $C^{(\text{HF})}$ in Eq. (3).

In Eq. (6), the linear part of control is represented by a linear transfer function $\Phi(j\omega)$, whereas the nonlinear part is determined by the parameter G_{NL} . For the linear part, $\Phi(j\omega)$ is used to tailor the impedance properties of the loudspeaker,

$$\Phi = \frac{S_d}{Bl} \cdot \beta \frac{Z_{\text{st}}(j\omega) - Z_s(j\omega)}{Z_{\text{st}}(j\omega)}. \quad (7)$$

It targets a specific acoustic impedance $Z_{\text{st}}^{(\text{F})}$ with two degrees of freedom,

$$Z_{\text{st}}^{(\text{F})} = \frac{Z_{\text{st}} Z_s}{(1 - \beta) Z_{\text{st}} + \beta Z_s} = \left[\frac{1 - \beta}{Z_{\text{st}}} + \frac{\beta}{Z_s} \right]^{-1}, \quad (8)$$

in which the control-designed impedance Z_{st} is made in parallel with the passive one Z_s . They possess different weights adjusted by the constant parameter β . Z_{st} corresponds to a one-degree-of-freedom resonator, as reported earlier⁶⁰.

For the control execution, there exists a time delay τ from control inputs to outputs, which is unavoidable in reality. It is taken into account in simulating practical case by transforming $i(t)$ into $i(t - \tau)$ for Eq. (5), and is experimentally determined at $100 \mu\text{s}$. Since the loudspeakers are naturally different, the control time delay affects them differently, yielding discrepancies in control results. Nevertheless, the addition of the parameter β in the linear control law allows such an issue to be compensated for in experiments, by balancing between Z_{st} and Z_s . As for the nonlinear part of the control law in Eq. (6), when the sub-wavelength cavity V_a between adjacent loudspeakers exhibits predominantly capacitor characteristics, we have $p_f = b_{n-1}$ and $p_b = a_n$ for loudspeakers with even indexes, and $p_f = a_n$ and $p_b = b_n$ for those with odd indexes. In this case, the nonlinear laws perfectly achieve the generators V_{2k-1}^{NL} and V_{2k}^{NL} required in the theoretical lattice in Fig. 2a.

Performing the above hybrid (linear and nonlinear) control on each loudspeaker, they all become Active Electroacoustic Resonators⁶⁰⁻⁶³ (labeled with AER_n in Fig. 3a), presenting the desired properties for realizing HF_n . A low level of less than 1 Pa is maintained for system excitation. It ensures the linear behaviors of the loudspeakers in the passive regime. Thus, nonlinearity is generated and tuned in an exact way, i.e., through the active control only (using the constant parameter G_{NL} in the control law). The detailed experimental results of nonlinear topological edge states are provided in Extended Data Figs. 5 and 6, in

which the amplitudes of each site are measured by microphones below Helmholtz resonators, as indicated in Fig. 3a.

DATA AVAILABILITY

The data underlying all figures will be made available on a public repository prior to the official publication date of this article.

REFERENCES

- ¹M. Z. Hasan and C. L. Kane, “Colloquium: Topological insulators,” *Rev. Mod. Phys.* **82**, 3045–3067 (2010).
- ²S. N. Kempkes, M. R. Slot, J. J. van den Broeke, P. Capiod, W. A. Benalcazar, D. Vanmaekelbergh, D. Bercioux, I. Swart, and C. M. Smith, “Robust zero-energy modes in an electronic higher-order topological insulator,” *Nat. Mater.* **18**, 1292–1297 (2019).
- ³S. Imhof, C. Berger, F. Bayer, J. Brehm, L. W. Molenkamp, T. Kiessling, F. Schindler, C. H. Lee, M. Greiter, T. Neupert, and R. Thomale, “Topoelectrical-circuit realization of topological corner modes,” *Nat. Phys.* **14**, 925–929 (2018).
- ⁴Y. Hadad, J. C. Soric, A. B. Khanikaev, and A. Alù, “Self-induced topological protection in nonlinear circuit arrays,” *Nat. Electron* **1**, 178–182 (2018).
- ⁵F. Zangeneh-Nejad and R. Fleury, “Nonlinear second-order topological insulators,” *Phys. Rev. Lett.* **123**, 053902 (2019).
- ⁶T. Ozawa, H. M. Price, A. Amo, N. Goldman, M. Hafezi, L. Lu, M. C. Rechtsman, D. Schuster, J. Simon, O. Zilberberg, and I. Carusotto, “Topological photonics,” *Rev. Mod. Phys.* **91**, 015006 (2019).
- ⁷A. B. Khanikaev, S. H. Mousavi, W.-K. Tse, M. Kargarian, A. H. MacDonald, and G. Shvets, “Photonic topological insulators,” *Nat. Mater.* **12**, 233–239 (2013).
- ⁸M. Serra-Garcia, V. Peri, R. Süsstrunk, O. R. Bilal, T. Larsen, L. G. Villanueva, and S. D. Huber, “Observation of a phononic quadrupole topological insulator,” *Nature* **555**, 342–345 (2018).
- ⁹G. G. Pyrialakos, N. Schmitt, N. S. Nye, M. Heinrich, N. V. Kantartzis, A. Szameit, and D. N. Christodoulides, “Symmetry-controlled edge states in the type-ii phase of dirac

- photonic lattices,” *Nat. Commun.* **11**, 2074 (2020).
- ¹⁰D. Smirnova, D. Leykam, Y. Chong, and Y. Kivshar, “Nonlinear topological photonics,” *Appl. Phys. Rev.* **7**, 021306 (2020).
- ¹¹G. Ma, M. Xiao, and C. T. Chan, “Topological phases in acoustic and mechanical systems,” *Nat. Rev. Phys.* **1**, 281–294 (2019).
- ¹²H. Xue, Y. Yang, and B. Zhang, “Topological acoustics,” *Nat. Rev. Mater.* **7**, 974–990 (2022).
- ¹³Z. Yang, F. Gao, X. Shi, X. Lin, Z. Gao, Y. Chong, and B. Zhang, “Topological acoustics,” *Phys. Rev. Lett.* **114**, 114301 (2015).
- ¹⁴S. D. Huber, “Topological mechanics,” *Nat. Phys.* **12**, 621–623 (2016).
- ¹⁵A. Souslov, B. C. van Zuiden, D. Bartolo, and V. Vitelli, “Topological sound in active-liquid metamaterials,” *Nat. Phys.* **13**, 1091–1094 (2017).
- ¹⁶C. He, X. Ni, H. Ge, X.-C. Sun, Y.-B. Chen, M.-H. Lu, X.-P. Liu, and Y.-F. Chen, “Acoustic topological insulator and robust one-way sound transport,” *Nat. Phys.* **12**, 1124–1129 (2016).
- ¹⁷D. Wang, Y. Deng, J. Ji, M. Oudich, W. A. Benalcazar, G. Ma, and Y. Jing, “Realization of a π -classified chiral-symmetric higher-order topological insulator in a coupling-inverted acoustic crystal,” *Phys. Rev. Lett.* **123**, 053902 (2019).
- ¹⁸H. Xue, Y. Yang, F. Gao, Y. Chong, and B. Zhang, “Acoustic higher-order topological insulator on a kagome lattice,” *Nat. Mater.* **18**, 108–112 (2019).
- ¹⁹F. Zangeneh-Nejad and R. Fleury, “Disorder-induced signal filtering with topological metamaterials,” *Adv. Mater.* **32**, 2001034 (2020).
- ²⁰A. Coutant, A. Sivadon, L. Zheng, V. Achilleos, O. Richoux, G. Theocharis, and V. Pagneux, “Acoustic su-schrieffer-heeger lattice: Direct mapping of acoustic waveguides to the su-schrieffer-heeger model,” *Phys. Rev. B* **103**, 224309 (2021).
- ²¹S. Shankar, A. Souslov, M. J. Bowick, M. C. Marchetti, and V. Vitelli, “Topological active matter,” *Nat. Rev. Mater.* **4**, 380–398 (2022).
- ²²X. Zhang, F. Zangeneh-Nejad, Z.-G. Chen, M.-H. Lu, and J. Christensen, “A second wave of topological phenomena in photonics and acoustics,” *Nature* **618**, 687–697 (2023).
- ²³D. A. Dobrykh, A. V. Yulin, A. P. Slobozhanyuk, A. N. Poddubny, and Y. S. Kivshar, “Nonlinear control of electromagnetic topological edge states,” *Phys. Rev. Lett.* **121**, 163901 (2018).

- ²⁴Y. Wang, L.-J. Lang, C. H. Lee, B. Zhang, and Y. D. Chong, “Topologically enhanced harmonic generation in a nonlinear transmission line metamaterial,” *Nat. Commun.* **10**, 1102 (2019).
- ²⁵M. Serra-Garcia, R. Süsstrunk, and S. D. Huber, “Observation of quadrupole transitions and edge mode topology in an lc circuit network,” *Phys. Rev. B* **99**, 020304 (2019).
- ²⁶L. J. Maczewsky, M. Heinrich, M. Kremer, S. K. Ivanov, M. Ehrhardt, F. Martinez, Y. V. Kartashov, V. V. Konotop, L. Torner, D. Bauer, and A. Szameit, “Nonlinearity-induced photonic topological insulator,” *Science* **370**, 701–704 (2020).
- ²⁷S. Mukherjee and M. C. Rechtsman, “Observation of floquet solitons in a topological bandgap,” *Science* **368**, 856–859 (2020).
- ²⁸Z. Hu, D. Bongiovanni, D. Jukić, E. Jajtić, S. Xia, D. Song, J. Xu, R. Morandotti, H. Buljan, and Z. Chen, “Nonlinear control of photonic higher-order topological bound states in the continuum,” *Light Sci. Appl.* **10**, 164 (2021).
- ²⁹D. D. Snee and Y.-P. Ma, “Edge solitons in a nonlinear mechanical topological insulator,” *Extreme Mech. Lett.* **30**, 100487 (2019).
- ³⁰P.-W. Lo, C. D. Santangelo, B. G.-g. Chen, C.-M. Jian, K. Roychowdhury, and M. J. Lawler, “Topology in nonlinear mechanical systems,” *Phys. Rev. Lett.* **127**, 076802 (2021).
- ³¹R. Chaunsali and G. Theocharis, “Self-induced topological transition in phononic crystals by nonlinearity management,” *Phys. Rev. B* **100**, 014302 (2019).
- ³²A. Darabi and M. J. Leamy, “Tunable nonlinear topological insulator for acoustic waves,” *Phys. Rev. Appl.* **12**, 044030 (2019).
- ³³R. Chaunsali, H. Xu, J. Yang, P. G. Kevrekidis, and G. Theocharis, “Stability of topological edge states under strong nonlinear effects,” *Phys. Rev. B* **103**, 024106 (2021).
- ³⁴S. Xia, D. Kaltsas, D. Song, I. Komis, J. Xu, A. Szameit, H. Buljan, K. G. Makris, and Z. Chen, “Nonlinear tuning of pt symmetry and non-hermitian topological states,” *Science* **372**, 72–76 (2021).
- ³⁵Y. Hadad, A. B. Khanikaev, and A. Alù, “Self-induced topological transitions and edge states supported by nonlinear staggered potentials,” *Phys. Rev. B* **93**, 155112 (2016).
- ³⁶A. Bisianov, M. Wimmer, U. Peschel, and O. A. Egorov, “Stability of topologically protected edge states in nonlinear fiber loops,” *Phys. Rev. A* **100**, 063830 (2019).
- ³⁷D. A. Smirnova, L. A. Smirnov, D. Leykam, and Y. S. Kivshar, “Topological edge states and gap solitons in the nonlinear dirac model,” *Laser Photonics Rev* **13**, 1900223 (2019).

- ³⁸T. Tuloup, R. W. Bomantara, C. H. Lee, and J. Gong, “Nonlinearity induced topological physics in momentum space and real space,” *Phys. Rev. B* **102**, 115411 (2020).
- ³⁹M. S. Kirsch, Y. Zhang, M. Kremer, L. J. Maczewsky, S. K. Ivanov, Y. V. Kartashov, D. B. Lluís Torner, A. Szameit, and M. Heinrich, “Nonlinear second-order photonic topological insulators,” *Nat. Phys.* **17**, 995–1000 (2021).
- ⁴⁰B.-U. Sohn, Y.-X. Huang, J. W. Choi, G. F. R. Chen, D. K. T. Ng, S. A. Yang, and D. T. H. Tan, “A topological nonlinear parametric amplifier,” *Nat. Commun.* **13**, 7218 (2022).
- ⁴¹B. M. Manda, V. Achilleos, O. Richoux, C. Skokos, and G. Theocharis, “Wave-packet spreading in the disordered and nonlinear su-schrieffer-heeger chain,” *Phys. Rev. B* **107**, 184313 (2023).
- ⁴²R. Chaunsali, P. G. Kevrekidis, D. Frantzeskakis, and G. Theocharis, “Dirac solitons and topological edge states in the β -fermi-pasta-ulam-tsingou dimer lattice,” *Phys. Rev. E* **108**, 054224 (2023).
- ⁴³J. Rogel-Salazar, “The gross-pitaevskii equation and bose-einstein condensates,” *Eur. J. Phys.* **34**, 247 (2013).
- ⁴⁴D. Leykam and Y. D. Chong, “Edge solitons in nonlinear-photonic topological insulators,” *Phys. Rev. Lett.* **117**, 143901 (2016).
- ⁴⁵Y. Hadad, V. Vitelli, and A. Alu, “Solitons and propagating domain walls in topological resonator arrays,” *ACS Photonics* **4**, 1974–1979 (2017).
- ⁴⁶S. Kruk, A. Poddubny, D. Smirnova, L. Wang, A. Slobozhanyuk, A. Shorokhov, I. Kravchenko, B. Luther-Davies, and Y. Kivshar, “Nonlinear light generation in topological nanostructures,” *Nat. Nanotechnol* **14**, 126–130 (2019).
- ⁴⁷D. Smirnova, S. Kruk, D. Leykam, E. Melik-Gaykazyan, D.-Y. Choi, and Y. Kivshar, “Third-harmonic generation in photonic topological metasurfaces,” *Phys. Rev. Lett.* **123**, 103901 (2019).
- ⁴⁸Z. Lan, J. W. You, and N. C. Panoiu, “Nonlinear one-way edge-mode interactions for frequency mixing in topological photonic crystals,” *Phys. Rev. B* **101**, 155422 (2020).
- ⁴⁹H. Hohmann, T. Hofmann, T. Helbig, S. Imhof, H. Brand, L. K. Upreti, A. Stegmaier, A. Fritzsche, T. Müller, U. Schwingenschlögl, C. H. Lee, M. Greiter, L. W. Molenkamp, T. Kießling, and R. Thomale, “Observation of cnoidal wave localization in nonlinear topoelectric circuits,” *Phys. Rev. Res.* **5**, L012041 (2023).

- ⁵⁰C.-K. Chiu, J. C. Y. Teo, A. P. Schnyder, and S. Ryu, “Classification of topological quantum matter with symmetries,” *Rev. Mod. Phys.* **88**, 035005 (2016).
- ⁵¹D. Zhou, D. Z. Rocklin, M. Leamy, and Y. Yao, “Topological invariant and anomalous edge modes of strongly nonlinear systems,” *Nat. Commun.* **13**, 3379 (2022).
- ⁵²X. Ni, M. Weiner, A. Alù, and A. B. Khanikaev, “Observation of higher-order topological acoustic states protected by generalized chiral symmetry,” *Nat. Mater.* **18**, 113–120 (2019).
- ⁵³L. Jezequel and P. Delplace, “Nonlinear edge modes from topological one-dimensional lattices,” *Phys. Rev. B* **105**, 035410 (2022).
- ⁵⁴Z. Wang, X. Wang, Z. Hu, D. Bongiovanni, D. Jukić, L. Tang, D. Song, R. Morandotti, Z. Chen, and H. Buljan, “Sub-symmetry-protected topological states,” *Nat. Phys.* **19**, 992–998 (2023).
- ⁵⁵C. L. Kane and T. C. Lubensky, “Topological boundary modes in isostatic lattices,” *Nat. Phys.* **10**, 39–45 (2014).
- ⁵⁶V. Marinca and N. Herisanu, “The method of harmonic balance,” in *Nonlinear Dynamical Systems in Engineering: Some Approximate Approaches* (Springer Berlin Heidelberg, Berlin, Heidelberg, 2011) pp. 31–45.
- ⁵⁷X. Guo, V. E. Gusev, K. Bertoldi, and V. Tournat, “Manipulating acoustic wave reflection by a nonlinear elastic metasurface,” *J. Appl. Phys.* **123**, 124901 (2018).
- ⁵⁸X. Guo, V. E. Gusev, V. Tournat, B. Deng, and K. Bertoldi, “Frequency-doubling effect in acoustic reflection by a nonlinear, architected rotating-square metasurface,” *Phys. Rev. E* **99**, 052209 (2019).
- ⁵⁹E. Hairer, S. P. Norsett, and G. Wanner, “Runge-kutta and extrapolation methods,” in *Solving Ordinary Differential Equations I: Nonstiff Problems* (Springer Berlin Heidelberg, Berlin, Heidelberg, 1993) pp. 129–353.
- ⁶⁰E. Rivet, S. Karkar, and H. Lissek, “Broadband low-frequency electroacoustic absorbers through hybrid sensor-/shunt-based impedance control,” *IEEE Trans. Control Syst. Technol.* **25**, 63–72 (2017).
- ⁶¹X. Guo, H. Lissek, and R. Fleury, “Improving sound absorption through nonlinear active electroacoustic resonators,” *Phys. Rev. Appl.* **13**, 014018 (2020).
- ⁶²X. Guo, H. Lissek, and R. Fleury, “Observation of non-reciprocal harmonic conversion in real sounds,” *Commun. Physics.* **6**, 93 (2023).

⁶³M. Padlewski, M. Volery, R. Fleury, H. Lissek, and X. Guo, “Active acoustic su-schrieffer-heeger-like metamaterial,” *Phys. Rev. Appl.* **20**, 014022 (2023).

ACKNOWLEDGEMENTS

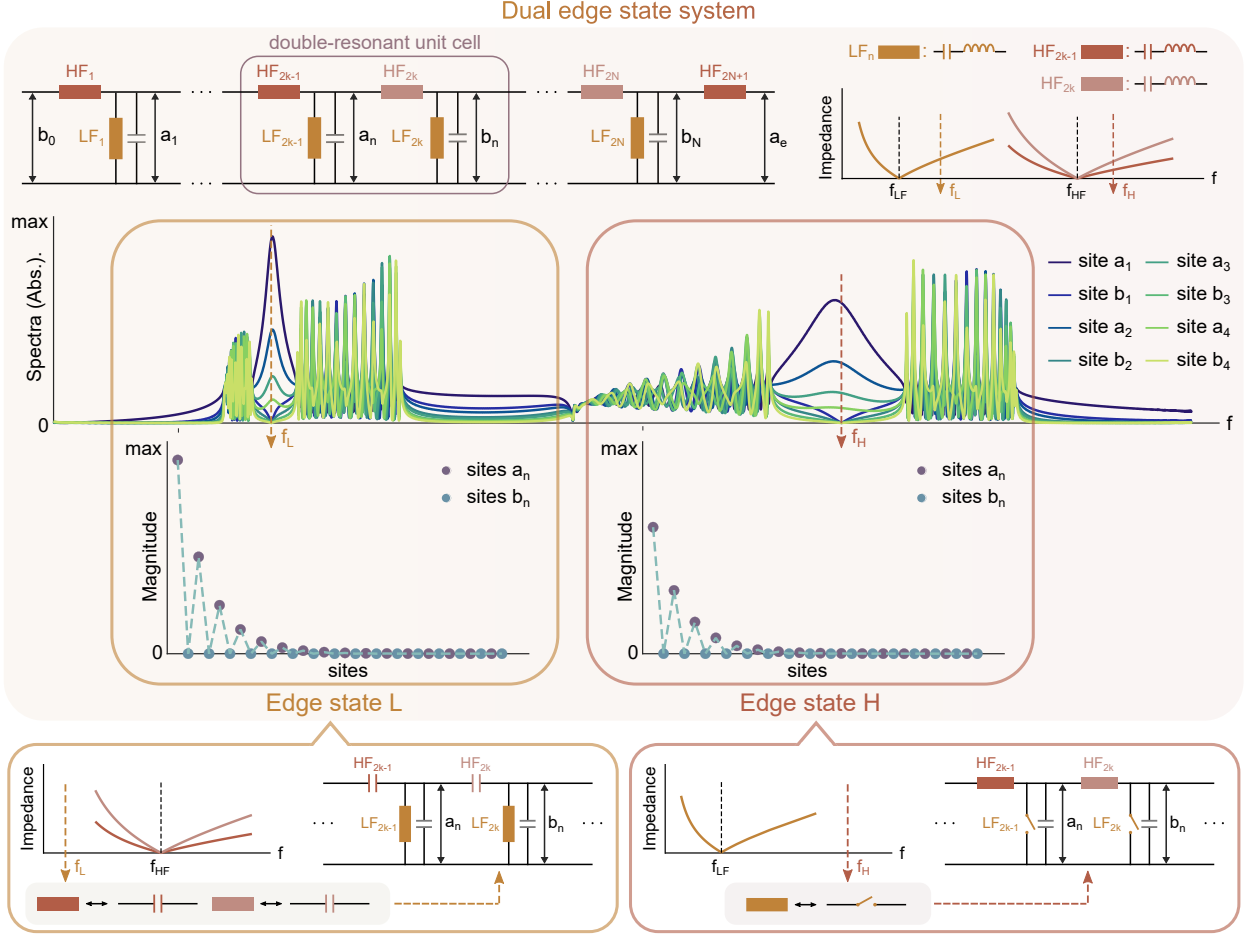
X.G., M.P., R.F., and H.L. acknowledge the Swiss National Science Foundation (SNSF) under grant No. 200020_200498. L.J. is funded by a PhD grant allocation Contrat doctoral Normalien.

AUTHOR CONTRIBUTIONS

R.F. and P.D. initiated and supervised the project. H.L. supervised the experimental work. X.G. established the theoretical modeling, performed the numerical simulations, designed the prototype, and carried out the measurements and data analysis. X.G. and M.P. set up the experiment. L.J. and P.D. developed the theory. X.G. and H.L. raised part of the funding that supported the experiment. All authors contributed to the writing of the manuscript and thoroughly discussed the results.

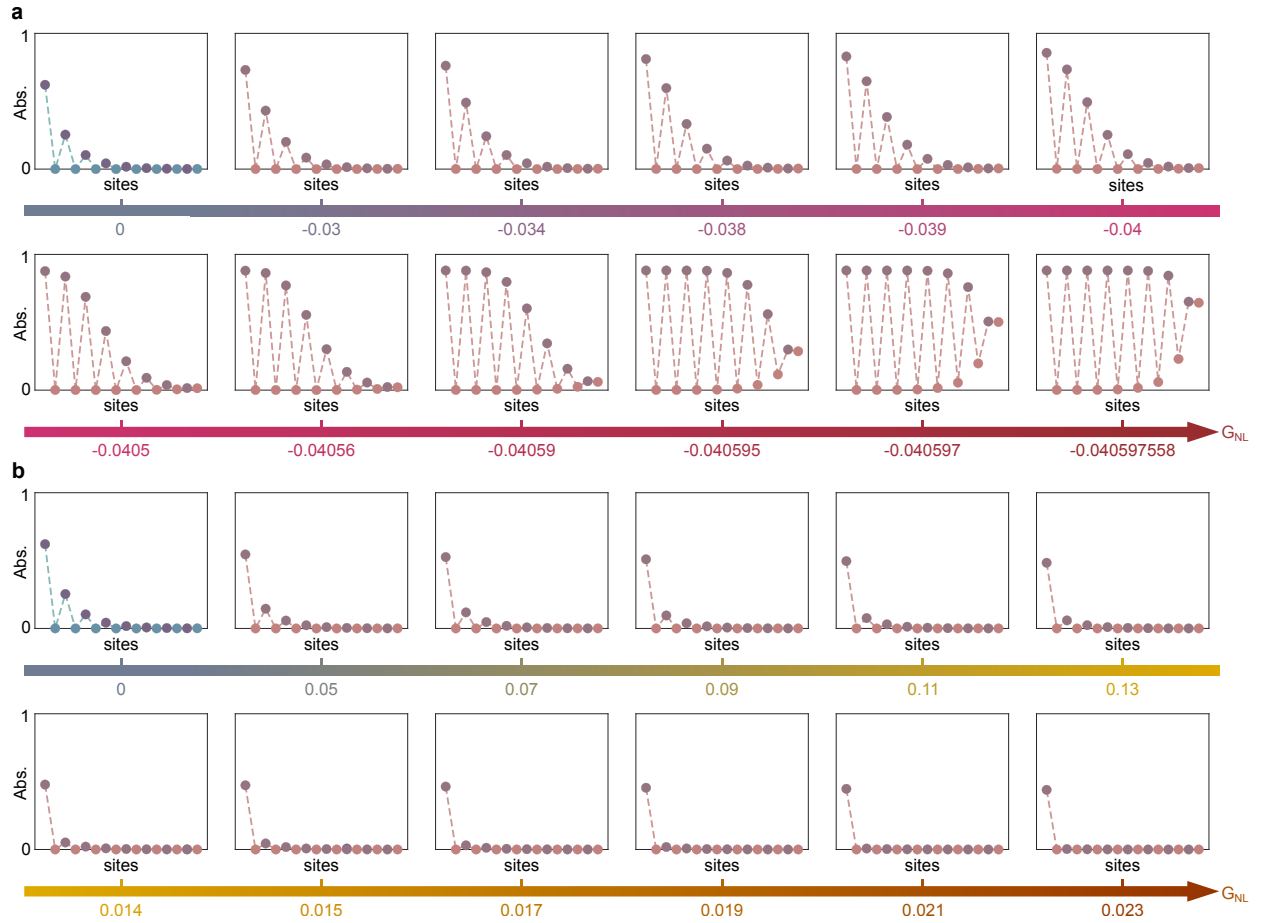
COMPETING INTERESTS

The authors declare no competing interests.

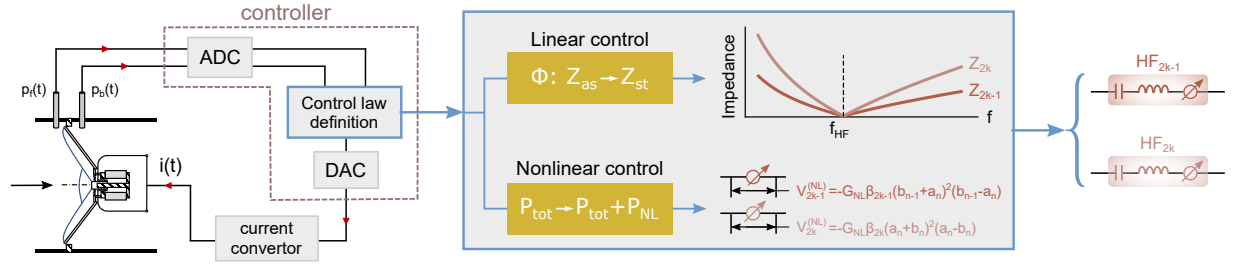


Extended Data Fig. 1. **Dual-band topological edge states in a single finite linear system.**

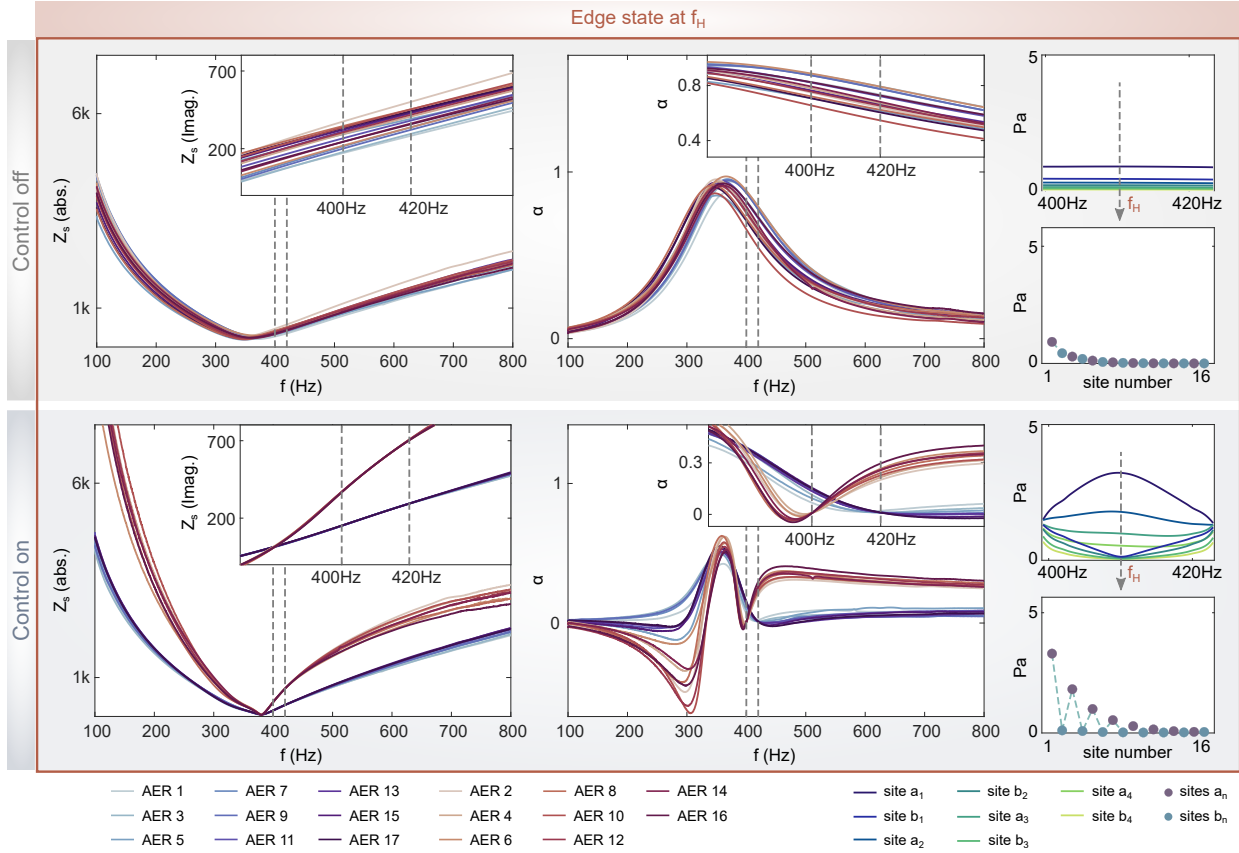
Each unit cell (with index n) of the system includes 2 types of resonators, (i) identical resonators LF_n ($n = 2k - 1$ and $2k$) resonating at a frequency f_{LF} , and (ii) resonators HF_n resonating at f_{HF} which is higher than that of the LF_n , but with different resonance bandwidths between odd (HF_{2k-1}) and even (HF_{2k}) ones. The whole system enables the generation of zero-energy topological edge states at two different frequencies, denoted as f_L and f_H , respectively. Indeed, since we impose $f_{LF} < f_{HF}$, the resonators HF_n exhibit mainly capacitance characteristics in the vicinity of f_{LF} , leading to the manifestation of only one resonance (of LF_n) in the unit cell. Similarly, when close to the frequency f_{HF} which is far from f_{LF} , the resonators LF_n have barely any impact, only the resonance of HF_n can act. Therefore, the system is equivalent to a classic topological lattice made of single-resonant unit cells in each circumstance, with the resonators connected either in parallel or in series through capacitors, as depicted herein.



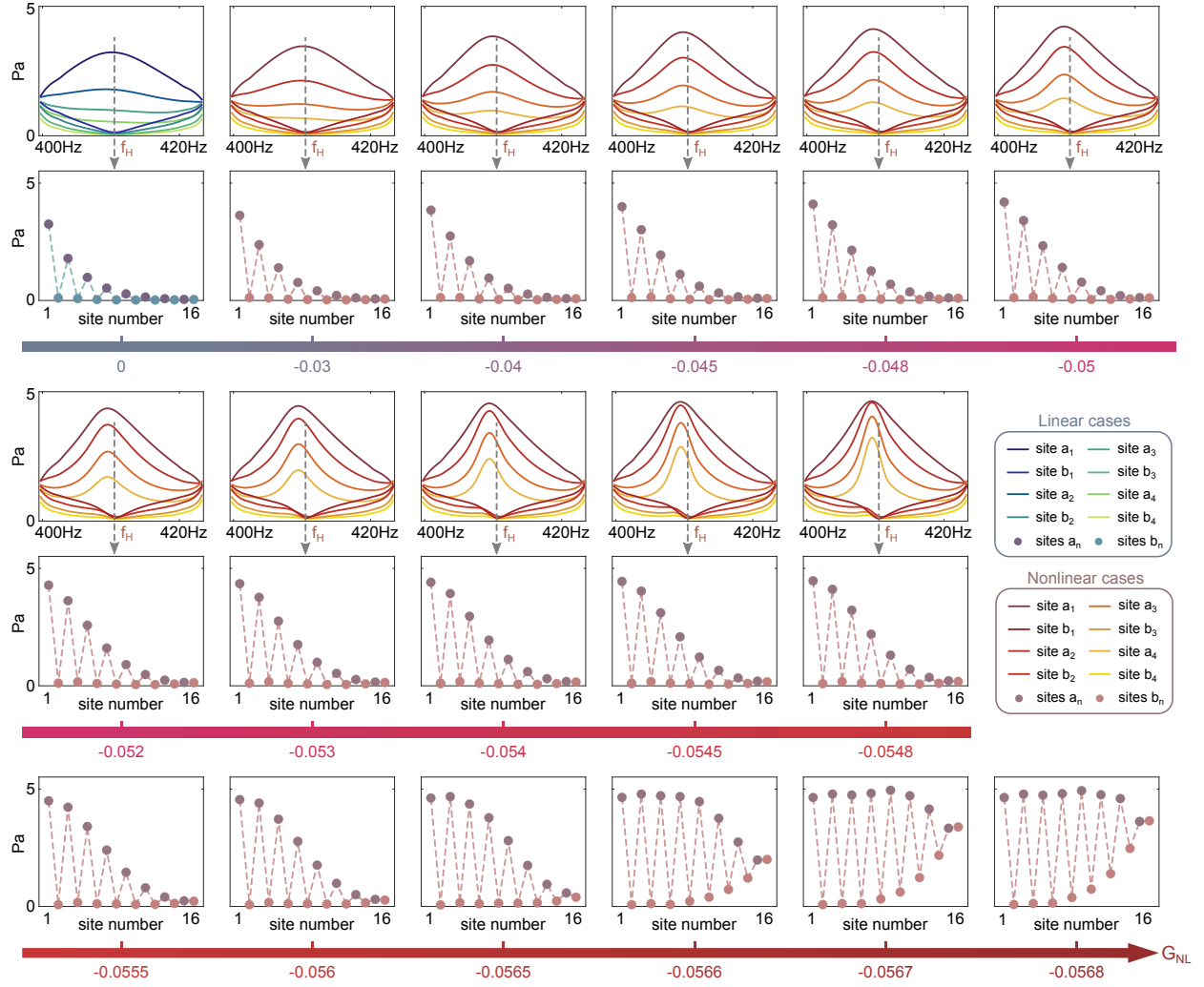
Extended Data Fig. 2. **Evolution of the chiral symmetry protected nonlinear topological edge states: detailed theoretical results.** The solutions are obtained with Harmonic Balance Method (see Method). The level of nonlinearity is tuned using the constant parameter G_{NL} , the value of which varies in the negative (a) and positive (b) directions, respectively. All inset figures are displayed within the same amplitude range as in Fig.2 in the main manuscript, while results of more nonlinear cases are showcased here.



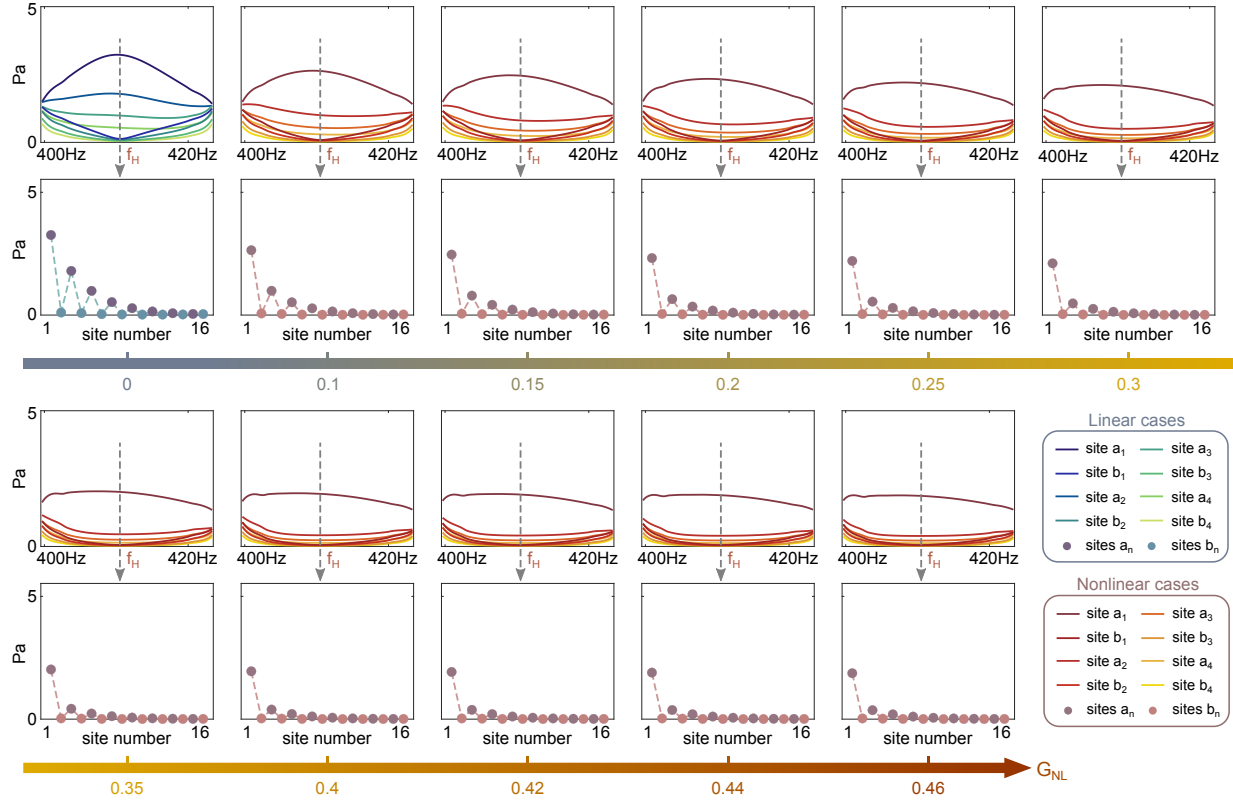
Extended Data Fig. 3. **Active control on the loudspeakers.** The linear part of the control is used for altering the impedance Z_n of each loudspeaker to make them resonate at the same frequency, while with different resonance bandwidths between odd and even ones. The nonlinear part of the control is for producing the nonlinear generators $V_n^{(NL)}$ needed in the theoretical lattice in Fig.2 in the main manuscript. ADC (DAC) denotes the Analog-Digital (Digital-Analog) Converter. The control time delay is mainly due to these AD and DA conversions that are unavoidable for the control law definition.



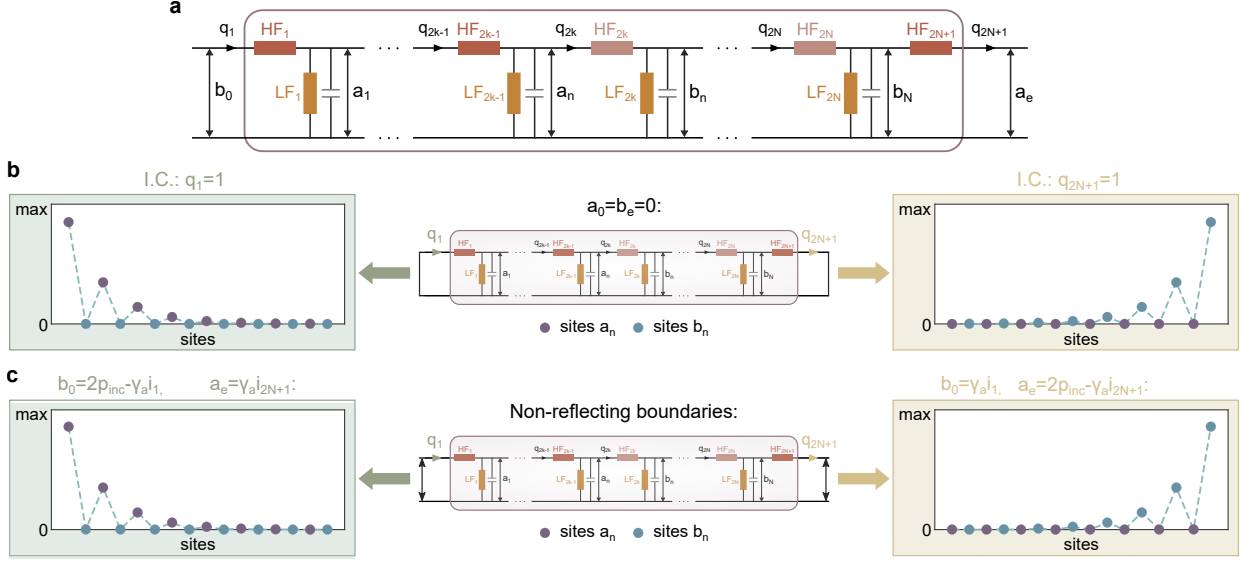
Extended Data Fig. 4. **Linear control results of topological edge state at f_H .** Comparison between the cases of control off and control on. The measured specific acoustic impedance Z_S and absorption coefficient α are also illustrated in both cases, for all the 17 loudspeakers in use. The edge state is generated only when the control is applied.



Extended Data Fig. 5. **Evolution of the chiral symmetry protected nonlinear topological edge states: detailed experimental results when $G_{NL} < 0$.** More results are given here compared to Fig.3 in the main manuscript.



Extended Data Fig. 6. **Evolution of the chiral symmetry protected nonlinear topological edge states: detailed experimental results when $G_{NL} > 0$.** More results are given compared to Fig.3 in the main manuscript.



Extended Data Fig. 7. **Identification of realizable boundary conditions.** **a**, The lumped element circuit considered, with b_0 and a_e the input and output boundaries, respectively. q_n designates the charge of the resonator HF_n . **b**, Zero-energy topological edge state at f_H derived with the closed-closed boundary conditions ($b_0 = a_e = 0$), and with a nonzero initial conditions of $q_1 \neq 0$ (left inset) or $q_{2N+1} \neq 0$ (right inset), respectively. **d**, Zero-energy topological edge state at f_H derived with the Non-Reflecting Boundary Conditions (NRBCs) for both ends of the system, where excitation is defined at each end, respectively. Based on an electro-acoustic analog where electrical (voltage, current) is equivalent to acoustic (pressure, flow), NRBCs are translated into $a_e = \gamma_a i_{2N+1}$ ($b_0 = \gamma_a i_1$) for the right (left) end of the system, in which i_{2N+1} (i_1) represents the current circulating in HF_1 (HF_{2N+1}), and $\gamma_a = Z_c/S$ with Z_c the specific acoustic impedance of the air and S the surface area of the propagation medium. The planar wave excitation at the left (right) end of the system can be expressed by the total pressure in the form of $b_0 = 2p_{\text{inc}} - \gamma_a i_1$ ($a_e = 2p_{\text{inc}} - \gamma_a i_{2N+1}$), with p_{inc} the incoming source that comes from infinity (there is no reflection in the direction of incidence). All the results are derived by the fourth-order Runge-Kutta time-integration method.